Journal of Biomedical Optics 9(6), 1271–1280 (November/December 2004)

Detection and diagnosis of oral neoplasia with an optical coherence microscope

A. L. Clark
University of Texas at Austin
Department of Biomedical Engineering
Austin, Texas 78712

A. Gillenwater
R. Alizadeh-Naderi
A. K. El-Naggar
University of Texas
M. D. Anderson Cancer Center
Departments of Head and Neck Surgery and Pathology
Houston, Texas

R. Richards-Kortum
University of Texas at Austin
Department of Biomedical Engineering
1 University Station C0800
Austin, Texas 78712
E-mail: kortum@mail.utexas.edu

Abstract. The use of high resolution, *in vivo* optical imaging may offer a clinically useful adjunct to standard histopathologic techniques. A pilot study was performed to investigate the diagnostic capabilities of optical coherence microscopy (OCM) to discriminate between normal and abnormal oral tissue. Our objective is to determine whether OCM, a technique combining the subcellular resolution of confocal microscopy with the coherence gating and heterodyne detection of optical coherence tomography, has the same ability as confocal microscopy to detect morphological changes present in precancers of the epithelium while providing superior penetration depths. We report our results using OCM to characterize the features of normal and neoplastic oral mucosa excised from 13 subjects. Specifically, we use optical coherence and confocal microscopic images obtained from human oral biopsy specimens at various depths from the mucosal surface to examine the optical properties that distinguish normal and neoplastic oral mucosa. An analysis of penetration depths achieved by the OCM and its associated confocal arm found that the OCM consistently imaged more deeply. Extraction of scattering coefficients from reflected nuclear intensity is successful in nonhyperkeratotic layers and shows differentiation between scattering properties of normal and dysplastic epithelium and invasive cancer. [DOI: 10.1117/1.1805558]

Keywords: optical imaging; optical coherence microscopy; oral dysplasia; amelanotic tissue; squamous cell carcinoma.

Paper 03135 received Nov. 18, 2003; revised manuscript received Apr. 1, 2004; accepted for publication Apr. 12, 2004.

1 Introduction

New optical imaging technologies can provide detailed images of tissue architecture and cellular morphology of living tissue. Optical coherence microscopy (OCM) is an exciting technique being developed that combines the subcellular resolution of high numerical aperture (NA) confocal microscopy with the increased sensitivity and penetration depth of optical coherence tomography (OCT) to noninvasively acquire detail similar to that available in histologic tissue evaluation. OCM images acquired from biological structures including plant specimens,[1,2] *in vitro* human colon tissue,[3] and human skin,[4] achieved a resolution of 2 μm[5] and a 200- to 500-μm field of view at a penetration depth of 600 μm. This suggests that OCM has the potential to image epithelial tissues with the subcellular resolution needed to assess their pathologic state.

OCM imaging builds detailed images of cell morphology and tissue architecture by using a high NA confocal microscope to collect light backscattered by various tissue components to provide contrast. The high NA objective focuses light to a 3-D voxel within the tissue, and a pinhole placed at a conjugate image plane within the confocal microscope allows light reflected from the focal volume to pass to the detector, while most light generated from out of focus points is blocked. Further rejection of out of focus light is achieved by using an interferometric gate to reject those photons that pass through the pinhole, but have not traveled the same optical pathlength as light generated at the focal volume, which has not undergone any further scattering events before exiting the tissue.[5,6] Changes in refractive index provide a source of reflected light at the image point, and the contrast necessary to recognize intracellular detail. Although OCM imaging has been limited to relatively few biological tissues, a review of results from confocal microscopy and OCT support the potential application of both optical modalities in the assessment of epithelial tissue.

Both confocal microscopy and OCT have successfully visualized precancerous and cancerous conditions in humans. High NA confocal microscopy with its subcellular resolution enables imaging of cell morphologic and tissue architectural changes associated with dysplasia and cancer. In skin, where cytoplasmic melanin provides a strong source of backscattering, confocal microscopes have captured morphologic changes in cytologic structure and visualized microvasculature in both basal cell carcinomas and melanomas.[7–10] In amelanotic epithelial tissues, where cell nuclei provide the primary source of reflected light, recent work showed that reflectance confocal imaging of normal and precancerous cervical tissue can characterize nuclear size, nuclear density, and

Address all correspondence to Rebecca Richards-Kortum, Univ. of Texas at Austin, ENS 610, Biomedical Engineering Program, Austin, TX 78712. Tel: 512-471-2104; Fax: 512-471-0616; E-mail: kortum@mail.utexas.edu; cc: anne.clark@mail.utexas.edu

1083-3668/2004/$15.00 © 2004 SPIE

nuclear-to-cytoplasmic ratio without the need for tissue sectioning or staining. In these studies, confocal images were used to discriminate high-grade cervical precancers with a sensitivity of 100% and a specificity of 91% in a study of 25 samples.[11] Similarly, nuclear-to-cytoplasmic differences from images of normal and esophageal cancer cells were used to identify cancer with a diagnostic accuracy of 90%.[12] Confocal imaging of oral mucosa has resolved subcellular detail at depths of 250 and 500 μm in the lip and tongue, respectively,[13] and oral squamous cell carcinoma from multiple sites.[14]

While high-resolution OCT imaging *in vitro* has demonstrated resolution on the order of 1 μm,[15] current clinically applicable OCT systems do not provide images with the subcellular resolution characteristic of high NA reflectance confocal microscopy. With penetration depth of up to 1 mm, OCT can resolve architectural differences associated with tissue from precancerous and cancerous specimens. In a study of the cervix, an OCT system was used to identify epithelial, basement membrane, and stromal changes characteristic of carcinoma *in situ* and invasive carcinoma.[16] In clinical trials, OCT endoscopes have also successfully imaged a large number of precancerous and invasive malignancies of different organs including the larynx, esophagus, uterine cervix, colon, urinary bladder, and esophagus[17–23] when compared to normal tissue. However, the spatial resolution of OCT is not sufficient to resolve cellular and subcellular morphology such as nuclear size.

To characterize the features of histologically normal and neoplastic oral mucosa, we conducted a pilot study using both a confocal microscope and an OCM system to image matched clinically normal and abnormal biopsies obtained from 13 patients. Our study shows that, like confocal microscopy, OCM can image and correctly characterize oral mucosal lesions with resolution comparable to histology without the need for tissue fixation, sectioning, or staining. In addition to subcellular resolution, the OCM demonstrated consistently deeper penetration than achieved by the confocal arm of the system. Analysis of epithelial scattering coefficients clearly discerns a difference between the hyperkeratotic layers and the nonkeratinized epithelium below, and an increase in scattering associated with premalignancy.

2 Methods and Materials

2.1 *Specimens*

Matched clinically normal and abnormal specimens were acquired from 13 patients at the Head and Neck Clinic of the University of Texas M. D. Anderson Cancer Center who were undergoing surgery for precancerous lesion or oral squamous cell carcinoma (SCC). Informed consent was given by all subjects, and the project was reviewed and approved by the University of Texas M. D. Anderson Cancer Center Office of Protocol Research and the Institutional Review Board at the University of Texas at Austin. Tissue biopsies (approximately 3 mm wide by 3 mm long by 2 mm thick) were taken from at least one clinically normal appearing and clinically suspicious area and immediately placed in growth medium (DMEM, no phenol red). A concerted effort was made to obtain tissue from early lesions, which are much more difficult to detect and diagnose clinically. Both optical coherence and reflectance confocal images were obtained at multiple image plane depths from the biopsies within 12 h of excision. Following imaging, biopsies were fixed in 10% formalin and submitted for routine histologic examination by an experienced head and neck pathologist. During this examination, a standard diagnosis form was used for each biopsy to record the pathologic state of the tissue sample (e.g., normal, dysplastic, or cancerous) and its differentiation (e.g., moderate versus well). The presence of keratinization and its extent and inflammation (both chronic and acute) as well as fibrosis, muscle, and salivary glands, was also noted. Additional sections from four of the biopsies were stained with monoclonal mouse anti-cytokeratin (Pan) (MMAC) concentrate antibody (Zymed Laboratories, Incorporated, San Francisco), a broad spectrum monoclonal antibody cocktail of clones A1 and A3 that reacts to cytokeratins 10, 14/15, 16, and 19 of the acidic and all members of the basic subfamily, to assess correlations between confocal image features and the presence of keratin in the specimen.

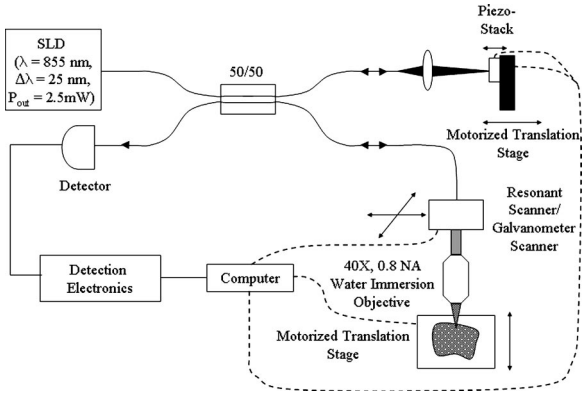

Fig. 1 Diagram of the OCM system used to image oral cavity specimens.

2.2 *Optical Coherence System*

Images were obtained from each biopsy using an OCM system (Fig. 1). Illumination was provided by a broadband superluminescent diode SLD 38 (Superlum Diodes, Limited, Moscow) operating at 850 nm with a 25-nm full-width half maximum (FWHM) bandwidth and delivered to the confocal microscope through a 50/50 coupler and a single-mode optical fiber. The illumination light was collimated to a beam diameter of 8 mm on exciting the optical fiber, and delivered to a water immersion microscope objective (40×, 0.8 NA) via a raster-scanning system. This scanning system used a resonant scanner providing an 85-Hz line scan rate and a slow scan galvanometer to move the focused light in the sample, allowing acquisition of images in 3 s. The objective focused light to a 1 μm-diam spot with an average illumination power of 0.4 mW. Light backscattered from the tissue was recoupled into the optical fiber, mixed in the 50/50 coupler with light returning from a reference arm, and sent to a low-noise, broadband detector 1801-FC (New Focus, San Jose, CA).

If the pathlengths of light returning from the sample and reference arm matched to within a coherence length of the SLD, interference fringes were produced at the detector. The pathlength of the reference light was small-amplitude (<1 μm) modulated using a technique described in Refs. 24 and

25, where light was reflected from a mirror mounted on a sinusoidally driven piezo AE0203D04 (NEC, Tokyo). Demodulation of the first two harmonics of this modulated signal allowed reduction and even elimination of variation in the signal caused by thermal drifts in the pathlengths of the reference and sample optical fibers.[3] Hoeling et al. demonstrated that the thermal variation could be eliminated if a modulation frequency of 122 kHz was used,[24] but to raise our image acquisition rate, we increased our modulation frequency to a resonant frequency at 376.65 kHz. At this higher frequency, the displacement of the mounted piezo per volt was too low to balance the two harmonics without damage to the piezo, but a driving signal of 7.5 $V_{p\text{-}p}$ was used to provide a peak-to-peak displacement of 315 nm and 65% reduction in phase variations. The resulting signal was amplified by 26 dB and bandpass filtered to isolate the two harmonics and reduce noise. A linear rms detector AD8361 (Analog, Norwood, MA) demodulated the signal and provided an estimate of signal intensity, or the square of the fringe amplitude. A complementary estimate of signal intensity was acquired by blocking the reference arm illumination and measuring the intensity of the backscattered light returned from the confocal microscope. This confocal signal returned to the computer through a separate electrical path, which bandpass filtered the signal to 250 kHz and provided 10 dB of amplification.

The OCM system operated at a dimensionless fiber spot size A[26] of 2.81 to optimize optical sectioning. The measured lateral and axial resolution of the system were 2.3 and 7.8 μm, respectively. The field of view was adjustable from 150 to 250 μm by controlling the deflection of the scan mirrors.

2.3 *Imaging and Image Processing*

Prior to imaging, the biopsies were removed from growth media, rinsed with phosphate buffered solution (PBS), and oriented so the image plane of the microscope was parallel to the epithelial surface and would approach the epithelial layer first. A 6% solution of acetic acid was then added to each sample to increase image contrast.[27] OCM and confocal image pairs were acquired at various epithelial depths until tissue details were no longer resolvable by either of the imaging modalities. On acquisition, image voltage data were saved to a file as floating point numbers and also translated into 8-bit, grayscale format using a full-scale contrast stretch algorithm to produce individual images. Additional postprocessing was performed on each of the image frames presented to increase image quality. Brightness was enhanced by adding a selected percentage of full grayscale to each pixel and contrast increased by removing another percentage of full grayscale from the image and expanding the remaining midrange gray levels.

Images of stained histologic sections were acquired using a color charge-coupled device (CCD) camera coupled to a brightfield microscope. The small field of view of the OCM made it difficult to register exactly where in the biopsy images were acquired; in each case we identified areas in histologic sections that corresponded to features present in our images.

2.4 *Scattering Coefficient Analysis*

A selection of image depth-of-focus stacks were also processed to estimate the epithelial tissue scattering coefficient using a technique described in Ref. 28. An estimate of the aggregate tissue scattering coefficient can be calculated using the equation,

$$I(z) = I_0 \exp(-\mu_t z) R(z) \exp(-\mu_t z)$$
$$= I_0 \exp(-2\mu_t z) R(z), \quad (1)$$

where I_0 is the irradiance at the depth z, at which the estimate begins, $R(z)$ is the depth-dependent reflectivity, and μ_t is the attenuation coefficient, which is the sum of the absorption and scattering coefficients. This technique assumes that excitation and reflected light travels parallel to the optical axis and that the attenuation coefficient does not vary as a function of depth. In the near infrared, where measurements were made, the absorption coefficient is significantly lower than the scattering coefficient,[29] so the attenuation coefficient was assumed to equal the scattering coefficient.

Binary masks outlining nuclei were hand-segmented by one person using the graphics editing program Paintshop (JASC, Eden Prarie, MN). A mean reflected intensity for these nuclei was calculated using the nuclear masks to extract specific voltage levels from the detector values saved during imaging and plotted as a function of depth for each stack. These data were fit to Eq. (1) by assuming that R was independent of depth and minimizing the mean square error between the data and the fit with the scattering coefficient as the only variable parameter.

Table 1 Number of clinically normal and abnormal biopsies from each site.

	Clinical appearance	
Location	Normal	Abnormal
Tongue (lateral and ventral surfaces)	3	4
Floor of mouth	2	2
Gingiva	4	6
Buccal mucosa	3	2
Soft palate	1	1

3 Results

3.1 *Imaging*

Both OCM and confocal images were successfully obtained from 28 biopsies with resolution similar to that provided by brightfield microscopy typically used for standard histopathologic evaluation. Table 1 shows the number of clinically normal and abnormal specimens obtained from each anatomic site within the oral cavity. Table 2 lists the histopathologic diagnoses for each biopsy from each subject. OCM images were acquired by scanning focused light in a plane parallel to the epithelial surface. Figure 2(f) shows a histology image from a biopsy with hyperkeratosis and hyperplasia from the floor of the mouth, flanked by confocal [Figs. 2(a) through 2(e)] and OCM [Figs. 2(g) through 2(k)] images taken from the same biopsy at the different depths indicated by the lines

Table 2 Histopathologic diagnosis by patient. The "None" diagnoses mean there was no epithelium in the specimen. The clinically normal (N) and abnormal (A) biopsies were acquired from different sites in the oral cavity due to the extent of the lesion.

		Histopathologic diagnosis	
No.	Site	Clinically normal biopsy	Clinically abnormal biopsy
1	Tongue (Lat. surface)	Hyperkeratosis, hyperplasia	Moderate focal dysplasia
2	Gingiva	Hyperkeratosis, hyperplasia	Hyperkeratosis, hyperplasia
3	Gingiva	Mild focal dysplasia	Moderate to severe focal dysplasia, hyperkeratosis
4	Gingiva	None	Hyperkeratosis, hyperplasia
5	Soft palate	Hyperkeratosis, hyperplasia	Well differentiated SCC
6	Floor of mouth (N) Gingiva (A)	Hyperkeratosis, hyperplasia	None
7	Tongue (Lat. surface)	Hyperkeratosis, hyperplasia	Mild focal dysplasia, hyperkeratosis
8	Floor of mouth	Mild dysplasia, hyperkeratosis	Mild to moderate dysplasia, severe hyperkeratosis
9	Tongue (Lat. surface)	Severe hyperkeratosis, hyperplasia	Mild dysplasia
10	Buccal mucosa (N,A1,A2)	Hyperkeratosis, hyperplasia	Severe hyperkeratosis (A1) hyperkeratosis, hyperplasia (A2)
11	Buccal mucosa (N) Floor of mouth (A1) Gingiva (A2)	Hyperkeratosis, hyperplasia	Moderate dysplasia, hyperkeratosis (A1) hyperkeratosis, hyperplasia, (A2)
12	Gingiva	Hyperkeratosis, hyperplasia	Moderately differentiated SCC
13	Buccal mucosa (N) Tongue (Lat. surface) (A)	Hyperkeratosis, hyperplasia	None

on Fig. 2(f). Images from the superficial epithelium [Figs. 2(a), 2(b), 2(g), and 2(h)] taken at 50 and 150 μm beneath the epithelial surface show larger cells with extensive keratin providing bright return from the cell periphery regions, while those acquired from 250 μm below the tissue surface [Figs. 2(c) and 2(i)] capture the more uniform, smaller cells associated with the intermediate layer. The images from the basal epithelium at 300 μm below the tissue surface [Figs. 2(d) and 2(j)] show a distinct increase in cell density and nuclear-to-cytoplasmic ratio, but contrast in the confocal image [Fig. 2(d)] is significantly reduced. At this depth, the OCM is still able to resolve cell membranes (arrow) [Fig. 2(j)], and at 350 μm below the tissue surface [Fig. 2(k)], basal cells are still visible in one portion of the image (arrow), while areas of low return represent where part of the image plane has traversed the basement membrane into stroma (double arrows). Confocal and OCM image features compare well with the corresponding transverse histologic section [Fig. 2(f)]. This pattern of confocal and OCM images was typical of those recorded from normal biopsies in this study.

Detection of oral dysplasia requires subcellular resolution to capture changes in nuclear shape and area characteristic of the pathologic changes in the squamous epithelium during malignant progression. Figure 3 shows both histologic and OCM images from a hyperplastic and hyperkeratotic mucosal specimen from gingiva [Figs. 3(a) and 3(c)] and invasive, well differentiated squamous cell carcinoma from the soft palate [Figs. 3(b) and 3(d)]. The nuclei in Figs. 3(a) and 3(c) manifest the regular and consistent features and spacing characteristic of healthy tissue. In sharp contrast, the tightly packed tumor cells imaged in Figs. 3(b) and 3(d) exhibit extensive variations in nuclear size and nuclear morphology. Epithelial nuclei (single arrows) appear as bright areas on the OCM image, whereas areas of stroma with inflammation (double arrows) appear dark in the OCM image.

3.2 *Penetration Depth and Scattering Coefficient Analysis*

An important performance measure for optical imaging in tissue is the maximum depth at which images can be obtained, or the penetration depth. Imaging performance for both modalities was analyzed for the 23 biopsies in which consistent features were resolved throughout imaging. For this analysis, penetration depth was defined as the maximum depth at which imaging captured individual nuclei. The results of this analysis are shown in Fig. 4. The OCM consistently imaged more deeply than the confocal microscope, imaging 100 μm deeper or more than confocal microscopy in 3 cases, 50 μm or more in 7 cases, and less than 50 μm deeper in 13 cases. Overall, the penetration depth of the OCM exceeded the penetration depth of the confocal by an average of 33%. The widely divergent penetration depths for the study (93 to 338 μm for the OCM) illustrate the challenge presented by the diversity of tissue types and pathologic states found in the oral cavity.

An analysis of epithelial scattering coefficients for these samples was also performed to investigate the clinical diagnostic potential of optical property changes associated with malignant progression. 29 depth-of-focus stacks, representing 16 biopsies, were selected. Stacks were chosen based on clarity of nuclei over at least five image depths and a maximum of two stacks per biopsy were used. In 23 of 29 stacks, an exponential curve could be fit to only a portion of the reflected nuclear intensity curve, because a region existed at the beginning of the data (most superficial layer) that did not fit the model. Reflectivities in these regions varied greatly with sig-

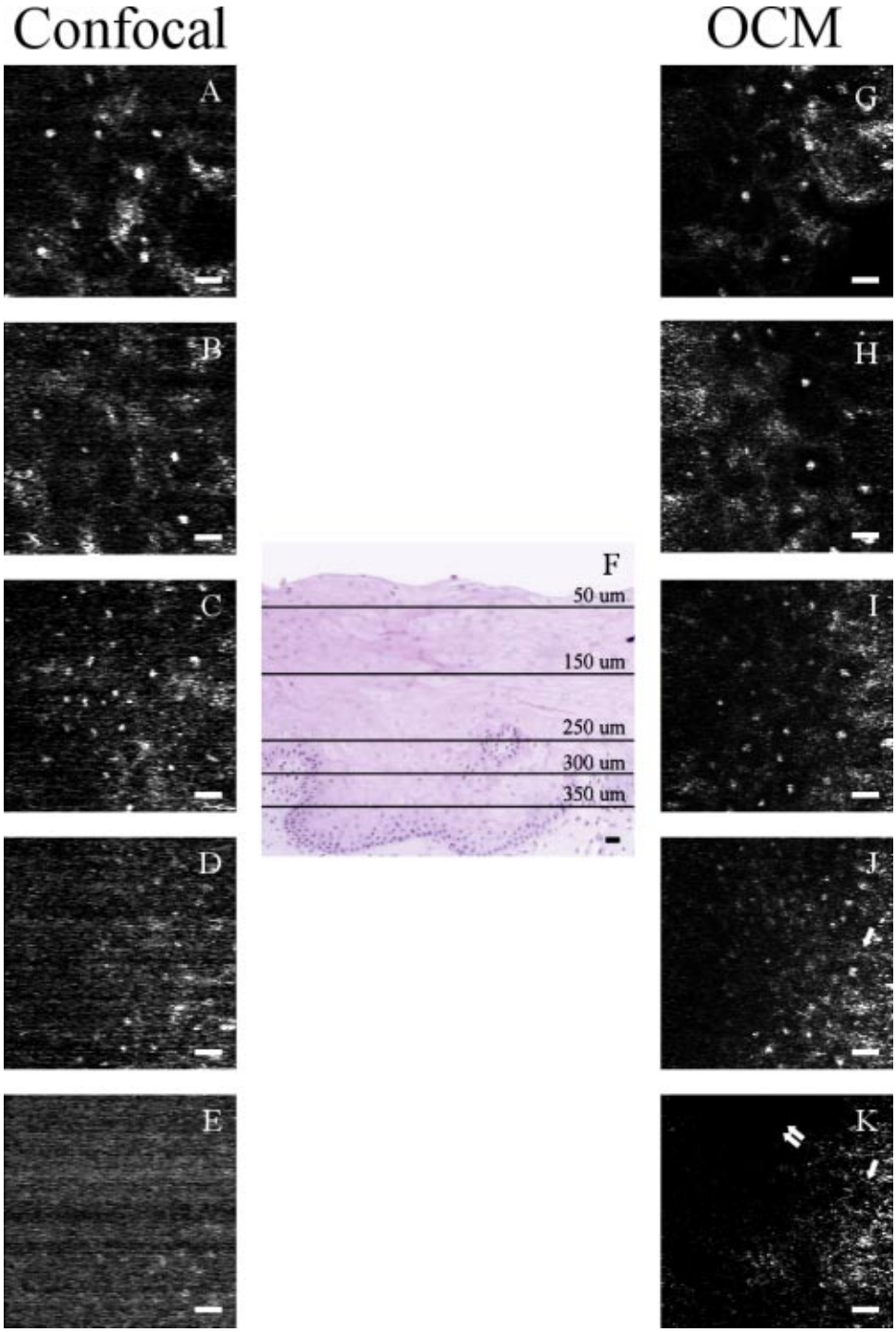

Fig. 2 Transverse histologic image (f) with en face confocal (a) through (e) and OCM (g) through (k) images obtained at different depths beneath the epithelial surface of a hyperkeratotic and hyperplastic floor of the mouth biopsy. Both imaging modalities captured an increase in nuclear density as the depth of the focal plane increased from (a) and (g) 50 μm to (b) and (h) 150 μm to (c) and (i) 250 μm below the tissue surface. At (d) 300 μm below the tissue surface, confocal image quality started to degrade and by (e), 350 μm below the tissue surface, features were barely resolvable. In the corresponding OCM images, cell membranes (arrow) are still resolvable at (j) 300 μm below the tissue surface. At (k) 350 μm below the tissue surface, cells are captured (arrow) and part of the focal plane has traversed through the basement membrane into stroma (double arrows). Scale bars=20 μm.

nal commonly increasing in the most superficial 20 to 50 μm before either remaining relatively constant or dropping off significantly. In 14 of the 23 stacks, the signal began to attenuate exponentially at a specific depth. The histopathologic evaluation of these cases showed that all 23 of these samples with the superficial zone characterized by variable reflectivity showed a hyperkeratotic epithelium. In contrast, five of the remaining six stacks were obtained from tissue with minimal

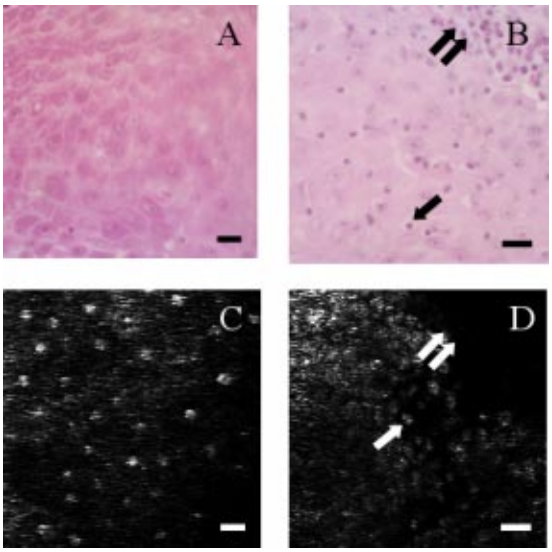

Fig. 3 Histologic and en face OCM images of normal and cancerous tissue. The consistent nuclear area and spacing in images from a hyperplastic and hyperkeratotic biopsy from gingiva (a) and (c) contrast sharply with the tightly packed tumor cells (arrow) containing irregular nuclei visualized in a well differentiated SCC from the soft palate (b) and (d). A portion of stroma with inflammation (double arrows) is also captured in both images (b) and (d) of the SCC. Scale bars=20 μm.

or no hyperkeratotic layer. Figure 5 shows the reflected nuclear intensity versus depth in two examples; the hyperkeratotic layers are clearly distinguishable in both the histology and the normalized nuclear reflectance plots. Figure 5(a) shows a histologic image from a keratin antibody (MMAC) stained section from a hyperkeratotic and hyperplastic gingiva biopsy, with a plot of normalized reflected nuclear intensity taken from the same biopsy shown in Fig. 5(b). The top 10 to 20 μm of the biopsy are heavily keratinized, followed by a 40 to 90 μm layer of keratinized cells. This layer is recorded in the plot by a brief period of increasing reflected nuclear intensity before the signal becomes relatively constant until 70 μm below the tissue surface. At this depth, the intensity begins to drop. When the data from 70 to 150 μm is fitted to an exponential curve, the fit constant is 54 (with an R^2 value of 0.91), implying a scattering coefficient of 27 cm^{-1}. The histologic image in Fig. 5(c) from a keratin antibody (MMAC) stained section from a hyperkeratotic, mildly dysplastic gingiva biopsy with focal moderate to severe dysplasia has a 20 to 40 μm heavily keratinized superficial layer above a 30 to 100 μm layer of keratinized cells. These keratinized layers are reflected in the plot in Fig. 5(d) by a brief period of increasing reflected nuclear intensity before the signal varies significantly until 120 μm below the tissue surface. At this depth, the intensity begins to drop. When the data from 120 to 190 μm is fitted to an exponential curve, the fit constant is 69 (with a R^2 value of 0.89), implying a scattering coefficient of 34 cm^{-1}.

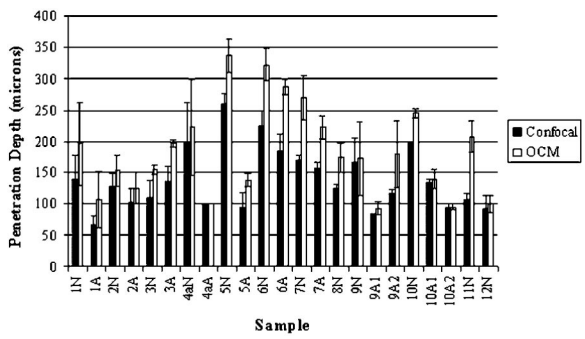

Fig. 4 Penetration depth of confocal microscopy versus OCM system.

Figure 6 shows more examples of normalized nuclear reflectance plots from different sites in the oral cavity representing multiple pathologic states. Variations in reflected nuclear intensities in the superficial layer of the measurements are also captured in Figs. 6(b) and 6(c). Figure 6 illustrates an increasing trend in scattering coefficients with increasing severity of neoplastic progression from normal to invasive SCC; a hyperkeratotic and hyperplastic biopsy [Fig. 6(a)], a hyperkeratotic, mildly dysplastic biopsy [Fig. 6(b)], a severely hyperkeratotic, moderately dysplastic biopsy [Fig. 6(c)], and an invasive, well-differentiated SCC [Fig. 6(d)] have estimated scattering coefficients of 16, 34, 48, and 70 cm^{-1}, respectively. This trend of increasing scattering coefficients is demonstrated in a scatter plot in Fig. 7(a) for the 20 samples that either did not have a hyperkeratotic region or had a second layer that exhibited an exponential attenuation of reflected nuclear intensity. Figure 7(b) shows the mean scattering coefficients for these stacks by pathologic diagnosis. The mean scattering coefficient for samples from normal biopsies was 27 ± 11 cm^{-1}, with a minimum and maximum value of 13 and 42 cm^{-1}, respectively. The mean scattering coefficient for samples from dysplastic biopsies was 39 ± 6 cm^{-1}, with a minimum and maximum value of 34 and 48 cm^{-1}, respectively. Finally, the mean scattering coefficient for samples from SCC biopsies was 60 ± 9 cm^{-1}, with a minimum and maximum value of 54 and 70 cm^{-1}, respectively. Thus, there is an increase in the average scattering coefficient as the tissue progresses from normal to dysplasia to cancer ($p<.05$, using a one-sided student's t-test), although further evaluation of this trend is needed due to the small number of samples with SCC.

4 Discussion

Our results illustrate the ability of OCM to image oral mucosa without tissue preparation and staining, with resolution comparable to histologic evaluation. Development of this technology for clinical evaluation of oral lesions in physicians and dental offices has potential to significantly enhance clinical management. In normal tissue, depth-related changes in cell diameter and nuclear density were observed at multiple anatomic sites within the oral cavity. The penetration depth of the OCM was greater than that which could be achieved with confocal microscopy. In SCCs, densely packed, pleomorphic tumor nuclei could be visualized, while areas of inflammation appeared dark. Our images correlate well with histology and are similar to previously reported optical imaging results in the oral cavity.[13,14]

Our oral epithelial scattering coefficient findings underscore the role that hyperkeratosis plays in optical imaging of the oral cavity. We postulate that the low levels of reflected

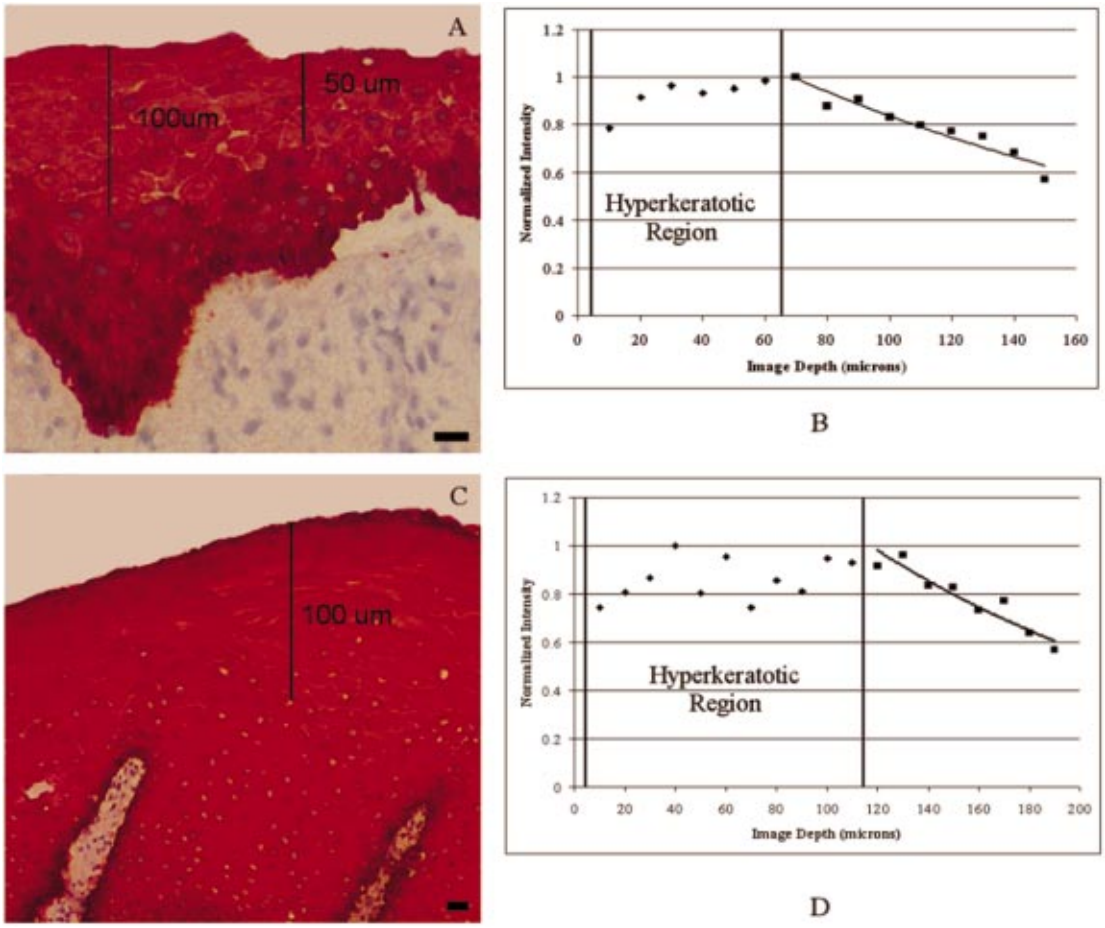

Fig. 5 Comparison of histology to normalized reflected nuclear intensity as a function of depth. (a) Histologic image from a keratin antibody (MMAC) stained section from a hyperkeratotic and hyperplastic gingiva biopsy. (b) Plot of normalized reflected nuclear intensity taken from the same biopsy in (a) showing characteristic decay within the hyperkeratotic region and exponential attenuation starting at 70 μm with a scattering coefficient of 27 cm^{-1}. (c) Histologic image from a keratin antibody (MMAC) stained section from a hyperkeratotic gingiva biopsy with mild dysplasia and focal moderate to severe dysplasia. (d) Plot of normalized reflected nuclear intensity taken from the same biopsy in (c) showing characteristic decay of the hyperkeratotic region and exponential attenuation starting at 120 μm with a scattering coefficient of 34 cm^{-1}.

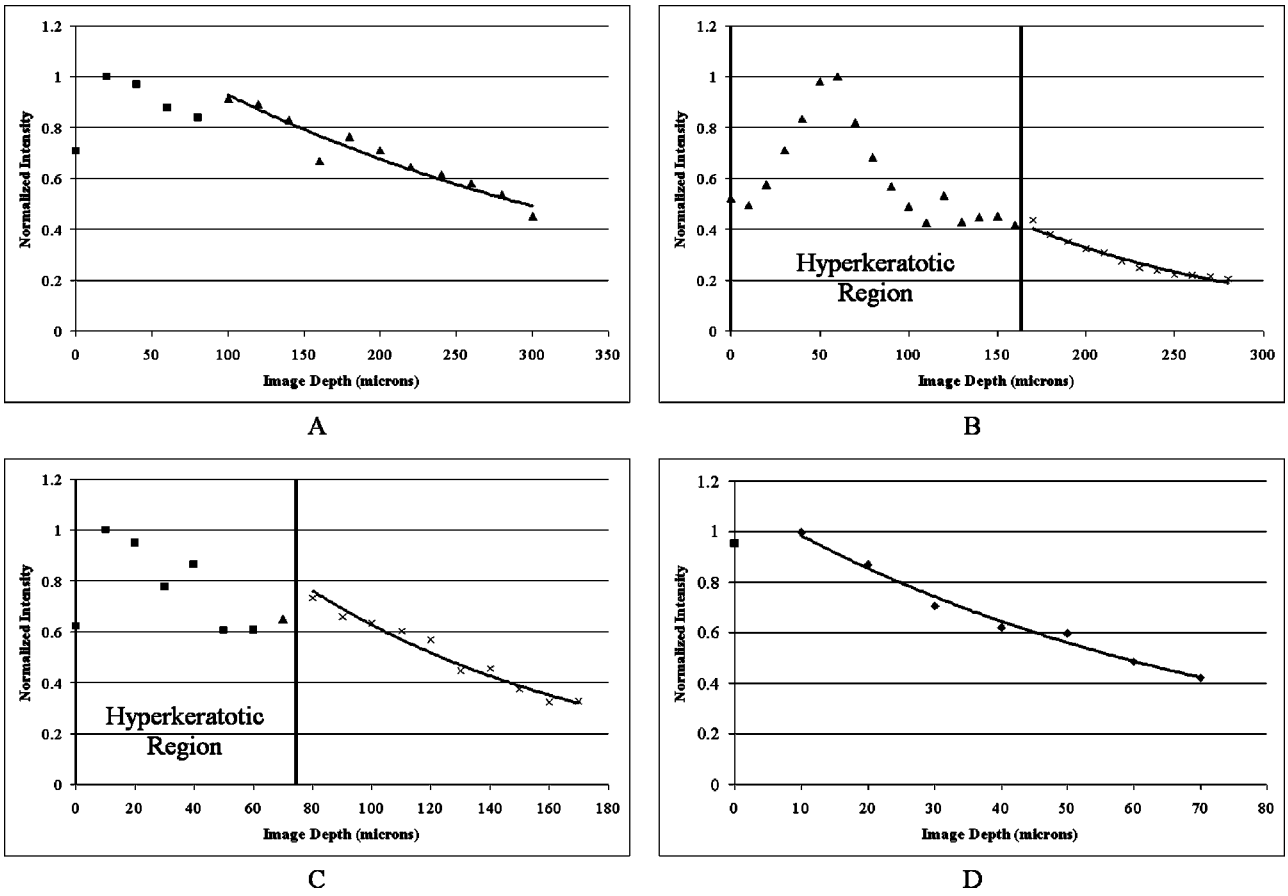

Fig. 6 Examples of normalized nuclear intensity plots from different sites and pathologic states. (a) Plot from a hyperkeratotic and hyperplastic biopsy from the floor of the mouth with an estimated scattering coefficient of 16 cm^{-1} (mean R^2 value of 0.92). (b) Plot from a hyperkeratotic, mildly dysplastic biopsy from the lateral surface of a tongue with an estimated scattering coefficient of 34 cm^{-1} (mean R^2 value of 0.96). (c) Plot from a severely hyperkeratotic, moderately dysplastic biopsy from the floor of the mouth with an estimated scattering coefficient of 48 cm^{-1} (mean R^2 value of 0.96). (d) Plot from an invasive, well-differentiated SCC from the soft palate with an estimated scattering coefficient of 70 cm^{-1} (mean R^2 value of 0.98).

intensity at the superficial portion of the hyperkeratotic layer and the characteristic depth-dependent reflectivities observed in the rest of the hyperkeratotic layer are a result of pyknotic nuclei. Previous studies have shown that chromatin material in the nucleus is responsible for the index mismatch that provides a significant amount of the contrast in optical imaging of amelanotic tissue.[30] Nuclei present in a hyperkeratotic (or parakeratotic) layer are pyknotic due to the cell death and the

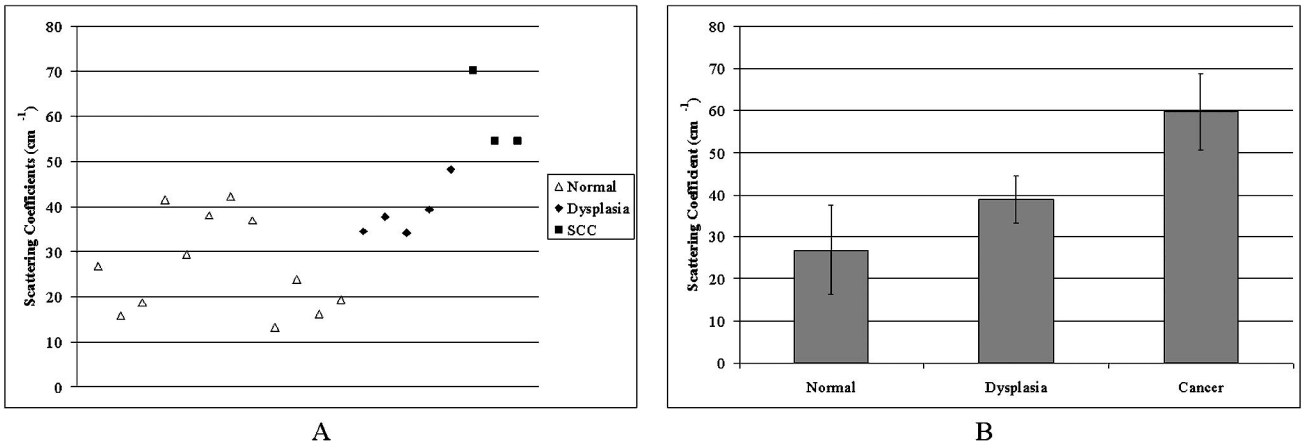

Fig. 7 (a) Scatter plot of scattering coefficients for nonhyperkeratotic tissue. (b) Bar chart comparing mean scattering coefficients for nonhyperkeratotic tissue by pathologic diagnosis.

consequent condensed and irregular chromatin.[31] Cellular pleomorphism and varying chromatin patterns will lead to fluctuation of reflectivity and scattering function.

The average scattering coefficients reported here show an increase from 27 cm^{-1} in normal tissue to 39 cm^{-1} in dysplastic tissue to 60 cm^{-1} in SCCs. We believe that the increased scattering in abnormal tissue is due to changes in nuclear morphology. Quantitative measures of normal oral epithelium and oral SCC find almost a doubling in DNA content in SCC when compared to normal tissue.[32] Our results are similar to the 22 and 69 cm^{-1} for normal and dysplastic epithelium, respectively, extracted from cervical tissue confocal images[28] and the 13 and 142 cm^{-1} for normal and dysplastic epithelium predicted by our finite difference time domain (FDTD) algorithm, which estimated the volume fraction of nuclei and average nuclear size from cervical confocal images.[33] We also observed higher scattering in normal oral mucosa than was found in cervical epithelium, which we attribute to higher levels of keratin in the oral cytoplasm.

The accuracy of the average scattering coefficients derived through this study is limited by certain assumptions made during data fitting to allow extraction of the average scattering coefficient as a single variable. First of all, it was assumed that the reflectance of nuclei is constant as a function of depth within the epithelium. FDTD models of the scattering cross section of superficial and basal epithelial cells have shown that this may not be the case, since increased nuclear optical density and increased refractive index heterogeneities within the nuclei cause increased backscattering from the basal cells.[33] In addition, the technique assumes that excitation and reflected light travels parallel to the optical axis, ignoring multiple scattering effects that begin to dominate signal return as the image plane traverses more deeply within the highly scattering tissue. Finally, we assume that the absorption coefficient is negligible compared to the scattering coefficient at 810 nm. This is likely reasonable, as the absorption coefficient of amelanotic epithelial tissues, including the cervix, has been reported with measurements below 1 cm^{-1}.[34]

Recently, a number of studies have suggested that optical spectroscopy and imaging can probe changes in both the epithelium and stroma of both oral and cervical tissue,[35–41] but to provide optimal diagnostic information, these methods must be based on accurate models of the optical properties of the target tissue. Our previous study of cervical epithelial scattering suggested, based on its results for epithelial scattering coefficients, that single layer models that assume tissue is homogeneous are not well suited to describe light propagation *in vivo* because of the large difference in scattering between epithelium and stroma.[28] Results reported here further emphasize this point by identifying separate layers within the epithelium with significantly different scattering properties. Therefore, techniques that attempt to accurately model microanatomical and biochemical features of epithelium and their effect on scattering[33,39,40,42] will play a vital role in supporting optical spectroscopy as a tool for noninvasive diagnosis in the oral cavity.

5 Conclusion

In this study, we demonstrate the power of optical coherence microscopy to visualize, at the subcellular level, features of both normal and neoplastic human oral mucosa. Penetration depths for the OCM are consistently greater than accompanying confocal imaging. Extraction of scattering coefficients from reflected nuclear intensity is successful in nonhyperkeratotic layers and shows differentiation between scattering properties of normal and dysplastic epithelium and SCCs. Our results suggest that OCM may enhance the ability of clinicians to noninvasively diagnose early oral lesions, and thus improve the management of persons at risk to develop oral cancer.

Acknowledgments

This research was supported by the National Institutes of Health (Grant No. 1 RO1 CA 82880-01).

References

1. J. W. Hettinger, M. de la Pena Mattozzi, W. R. Myers, M. E. Williams, A. Reeves, R. L. Parsons, R. C. Haskell, R. Wang, and J. I. Medford, ''Optical coherence microscopy. A technology for rapid, *in vivo*, non-destructive visualization of plants and plant cells,'' *Plant Physiol.* **123**, 3–15 (2000).
2. A. Reeves, R. L. Parsons, J. W. Hettinger, and J. I. Medford, ''In vivo three-dimensional imaging of plants with optical coherence microscopy,'' *J. Microsc.* **208**, 177–89 (2002).
3. J. A. Izatt, M. D. Kulkarni, H. W. Wang, K. Kobayashi, and M. V. Sivak, ''Optical coherence tomography and microscopy in gastrointestinal tissues,'' *IEEE J. Sel. Top. Quantum Electron.* **2**, 1017–1028 (1996).
4. A. D. Aguirre, P. Hsiung, T. H. Ko, I. Hartl, and J. G. Fujimoto, ''High-resolution optical coherence microscopy for high-speed, in vivo cellular imaging,'' *Opt. Lett.* **28**, 2064–2066 (2003).
5. J. A. Izatt, M. R. Hee, and G. M. Owen, ''Optical coherence microscopy in scattering media,'' *Opt. Lett.* **19**, 590 (1994).
6. C. L. Smithpeter, A. K. Dunn, A. J. Welch, and R. Richards-Kortum, ''Penetration depth limits of *in vivo* confocal reflectance imaging,'' *Appl. Opt.* **37**, 2749–2754 (1998).
7. K. J. Busam, K. Hester, C. Charles, D. L. Sachs, C. R. Antonescu, S. Gonzalez, and A. C. Halpern, ''Detection of clinically amelanotic malignant melanoma and assessment of its margins by *in vivo* confocal scanning laser microscopy,'' *Arch. Dermatol.* **137**, 923–929 (2001).
8. R. G. Langley, M. Rajadhyaksha, P. J. Dwyer, A. J. Sober, T. J. Flotte, and R. R. Anderson, ''Confocal scanning laser microscopy of benign and malignant melanocytic skin lesions *in vivo*,'' *J. Am. Acad. Dermatol.* **45**, 365–376 (2001).
9. S. Gonzalez and Z. Tannous, ''Real-time, *in vivo* confocal reflectance microscopy of basal cell carcinoma,'' *J. Am. Acad. Dermatol.* **47**, 869–874 (2002).
10. Z. S. Tannous, M. C. Mihm, T. J. Flotte, and S. González, ''*In vivo* examination of lentigo maligna and malignant melanoma *in situ*, lentigo maligna type by near-infrared reflectance confocal microscopy: Comparison of *in vivo* confocal images with histologic sections,'' *J. Am. Acad. Dermatol.* **46**, 260–263 (2002).
11. T. Collier, A. Lacy, R. Richards-Kortum, A. Malpica, and M. Follen, ''Near real-time confocal microscopy of amelanotic tissue: Detection of dysplasia in *ex vivo* cervical tissue,'' *Acad. Radiol.* **9**, 504–512 (2002).
12. H. Inoue, T. Igari, T. Nishikage, K. Ami, T. Yoshida, and T. Iwai, ''A novel method of virtual histopathology using laser-scanning confocal microscopy *in vitro* with untreated fresh specimens from the gastrointestinal mucosa,'' *Endoscopy* **32**, 439–443 (2000).
13. W. M. White, M. Rajadhyaksha, S. Gonzalez, R. L. Fabian, and R. R. Anderson, ''Noninvasive imaging of human oral mucosa *in vivo* by confocal reflectance microscopy,'' *Laryngoscope* **109**, 1709–1717 (1999).
14. A. Clark, A. M. Gillenwater, T. Collier, R. Alizadeh-Naderi, A. K. El-Naggar, and R. R. Richards-Kortum, ''Confocal microscopy for real time detection of oral cavity neoplasia,'' *Clinical Cancer Res.* **9**, 4714–4721 (2003).
15. W. Drexler, U. Morgner, F. X. Kartner, C. Pitris, S. A. Boppart, X. D. Li, E. P. Ippen, and J. G. Fujimoto, ''*In vivo* ultrahigh-resolution

optical coherence tomography,'' *Opt. Lett.* **24**, 1221–1223 (1999).
16. C. Pitris, A. Goodman, S. A. Boppart, J. J. Libus, J. G. Fujimoto, and M. E. Brezinski, ''High-resolution imaging of gynecologic neoplasms using optical coherence tomography,'' *Obstet. Gynecol. (N.Y., NY, U. S.)* **93**, 135–139 (1999).
17. G. Zuccaro, N. Gladkova, J. Vargo, F. Feldchtein, E. Zagaynova, D. Conwell, G. Falk, J. Goldblum, J. Dumot, J. Ponsky, G. Gelikonov, B. Davros, E. Donchenko, and J. Richter, ''Optical coherence tomography of the esophagus and proximal stomach in health and disease,'' *Am. J. Gastroenterol.* **96**, 2633–2639 (2001).
18. S. Jäckle, N. Gladkova, F. Feldchtein, A. Terentieva, B. Brand, G. Gelikonov, V. Gelikonov, A. Sergeev, A. Fritscher-Ravens, J. Freund, U. Seitz, S. Schröder, and N. Soehendra, ''*In vivo* endoscopic optical coherence tomography of esophagitis, Barrett's esophagus, and adenocarcinoma of the esophagus,'' *Endoscopy* **32**, 750–755 (2000).
19. S. Jäckle, N. Gladkova, F. Feldchtein, A. Terentieva, B. Brand, G. Gelikonov, V. Gelikonov, A. Sergeev, A. Fritscher-Ravens, J. Freund, U. Seitz, S. Soehendra, and N. Schrödern, ''*In vivo* endoscopic optical coherence tomography of the human gastrointestinal tract—toward optical biopsy,'' *Endoscopy* **32**, 743–749 (2000).
20. A. M. Sergeev, V. M. Gelikonov, G. V. Gelikonov, F. I. Feldchtein, R. V. Kuranov, and N. D. Gladkova, ''*In vivo* endoscopic OCT imaging of precancer and cancer states of human mucosa,'' *Opt. Express* **1**, 432–440 (1997).
21. B. E. Bouma, G. J. Tearney, C. C. Compton, and N. S. Nishioka, ''High-resolution imaging of the human esophagus and stomach in vivo using optical coherence tomography,'' *Gastrointest Endosc.* **51**(4), 467–474 (2000).
22. X. D. Li, S. A. Boppart, J. Van Dam, H. Mashimo, M. Mutinga, W. Drexler, M. Klein, C. Pitris, M. L. Krinsky, M. E. Brezinski, and J. G. Fujimoto, ''Optical coherence tomography: advanced technology for the endoscopic imaging of Barrett's esophagus,'' *Endoscopy* **32**, 921–930 (2000).
23. C. A. Jesser, S. A. Boppart, C. Pitris, D. L. Stamper, G. P. Nielsen, M. E. Brezinski, and J. G. Fujimoto, ''High resolution imaging of transitional cell carcinoma with optical coherence tomography: Feasibility for the evaluation of bladder pathology,'' *Br. J. Radiol.* **72**, 1170–1176 (1999).
24. B. M. Hoeling, A. D. Fernandez, R. C. Haskell, E. Huang, W. R. Myers, D. C. Peterson, S. E. Ungersma, R. Wang, and M. E. Williams, ''An optical coherence microscope for 3-dimensional imaging in developmental biology,'' *Opt. Express* **6**, 136–146 (2000).
25. B. M. Hoeling, A. D. Fernandez, R. C. Haskell, and D. C. Petersen, ''Phase modulation at 125 kHz in a Michelson interferometer using an inexpensive piezoelectric stack driven at resonance,'' *Rev. Sci. Instrum.* **72**, 1630–1633 (2001).
26. M. Gu, C. J. R. Sheppard, and X. Gan, ''Image formation in a fiber-optical confocal scanning microscope,'' *J. Opt. Soc. Am. A* **8**, 1755–1761 (1991).
27. R. A. Drezek, T. Collier, C. K. Brookner, A. Malpica, R. Lotan, R. R. Richards-Kortum, and M. Follen, ''Laser scanning confocal microscopy of cervical tissue before and after application of acetic acid,'' *Am. J. Obstet. Gynecol.* **182**, 1135–1139 (2000).
28. T. Collier, D. Arifler, R. Richards-Kortum, A. Malpica, and M. Follen, ''Determination of epithelial tissue scattering coefficient using confocal microscopy,'' *IEEE J. Sel. Top. Quantum Electron.* **9**, 307–313 (2003).
29. J. Qu, C. MacAuley, S. Lam, and B. Palcic, ''Optical properties of normal and carcinomatous bronchial tissue,'' *Appl. Opt.* **33**, 7397–7405 (1994).
30. C. L. Smithpeter, A. K. Dunn, R. Drezek, T. Collier, and R. Richards-Kortum, ''Near real time confocal microscopy of cultured amelanotic cells: Sources of signal, contrast agents, and limits of contrast,'' *J. Biomed. Opt.* **3**, 429–436 (1998).
31. S. L. Robbins, R. S. Cotran, and V. Kumar, *Pathologic Basis of Disease*, 3rd ed., W. B. Saunders, Philadelphia, PA (1984).
32. Y. Kinoshita, S. Inoue, Y. Honma, and K. Shimura, ''Diagnostic significance of nuclear DNA content and nuclear area in oral hyperplasia, dysplasia, and carcinoma,'' *J. Oral Maxillofac. Surg.* **50**, 728–733 (1992).
33. D. Arifler, M. Guillaud, A. Carraro, A. Malpica, M. Follen, and R. R. Richards-Kortum, ''Light scattering from normala and dysplastic cervical cells at different epithelial depths: finite-difference time-domain modeling with a perfectly matched layer boundary condition,'' *J. Biomed. Opt.* **8**, 484–494 (2003).
34. W. F. Cheong, S. A. Prahl, and A. J. Welch, ''A review of the optical properties of biological tissues,'' *IEEE J. Sel. Top. Quantum Electron.* **26**, 2166–2185 (1990).
35. A. Gillenwater, R. Jacob, and R. Richards-Kortum, ''Fluorescence spectroscopy: A technique with potential to improve the early detection of aerodigestive tract neoplasia,'' *Head Neck* **20**, 556–562 (1998).
36. C. Y. Wang, H. K. Chiang, C. T. Chen, C. P. Chiang, Y. S. Kuo, and S. N. Chow, ''Diagnosis of oral cancer by light-induced autofluorescence spectroscopy using double excitation wavelengths,'' *Oral Oncol.* **35**, 144–150 (1999).
37. A. Gillenwater, R. Jacob, R. Ganeshappa, B. Kemp, A. K. El-Naggar, J. L. Palmer, G. Clayman, M. F. Mitchell, and R. Richards-Kortum, ''Noninvasive diagnosis of oral neoplasia based on fluorescence spectroscopy and native tissue autofluorescence,'' *Arch. Otolaryngol. Head Neck Surg.* **124**, 1251–1258 (1998).
38. D. C. De Veld, M. Skurichina, M. J. Witjes, R. P. Duin, D. J. Sterenborg, W. M. Star, and J. L. Roodenburg, ''Autofluorescence characteristics of healthy oral mucosa at different anatomical sites,'' *Lasers Surg. Med.* **32**, 367–376 (2003).
39. I. Pavlova, K. Sokolov, R. Drezek, A. Malpica, M. Follen, and R. Richards-Kortum, ''Microanatomical and biochemical origins of normal and precancerous cervical autofluorescence using laser-scanning fluorescence confocal microscopy,'' *Photochem. Photobiol.* **77**, 550–555 (2003).
40. R. Drezek, C. Brookner, I. Pavlova, I. Boiko, A. Malpica, R. Lotan, M. Follen, and R. Richards-Kortum, ''Autofluorescence microscopy of fresh cervical-tissue sections reveals alterations in tissue biochemistry with dysplasia,'' *Photochem. Photobiol.* **73**, 636–641 (2001).
41. B. Kulapaditharom and V. Boonkitticharoen, ''Laser-induced fluorescence imaging in localization of head and neck cancers,'' *Ann. Otol. Rhinol. Laryngol.* **107**, 241–246 (1998).
42. R. Drezek, M. Guillaud, T. Collier, I. Boiko, A. Malpica, C. Macaulay, M. Follen, and R. Richards-Kortum, ''Light scattering from cervical cells throughout neoplastic progression: influence of nuclear morphology, DNA content, and chromatin texture,'' *J. Biomed. Opt.* **8**, 7–16 (2003).